What Controls the Deep Cycle? Proxies for Equatorial Turbulence

W. D. SMYTH,[a] S. J. WARNER,[a] J. N. MOUM,[a] H. T. PHAM,[b] AND S. SARKAR[b,c]

[a] College of Earth, Ocean and Atmospheric Sciences, Oregon State University, Corvallis, Oregon
[b] Department of Mechanical and Aerospace Engineering, University of California, San Diego, La Jolla, California
[c] Scripps Institution of Oceanography, University of California, San Diego, La Jolla, California

(Manuscript received 29 September 2020, in final form 19 April 2021)

ABSTRACT: Factors thought to influence deep cycle turbulence in the equatorial Pacific are examined statistically for their predictive capacity using a 13-yr moored record that includes microstructure measurements of the turbulent kinetic energy dissipation rate. Wind stress and mean current shear are found to be most predictive of the dissipation rate. Those variables, together with the solar buoyancy flux and the diurnal mixed layer thickness, are combined to make a pair of useful parameterizations. The uncertainty in these predictions is typically 50% greater than the uncertainty in present-day in situ measurements. To illustrate the use of these parameterizations, the record of deep cycle turbulence, measured directly since 2005, is extended back to 1990 based on historical mooring data. The extended record is used to refine our understanding of the seasonal variation of deep cycle turbulence.

KEYWORDS: Ocean dynamics; Atmosphere-ocean interaction; Diapycnal mixing; Mixing; Oceanic mixed layer

1. Introduction

The equator is a prime location for air–sea property fluxes. Especially active are the regions of low sea surface temperature in the eastern equatorial Pacific and Atlantic basins. In the context of climate, it matters greatly whether heat and other scalars absorbed in these regions are released quickly back to the atmosphere or carried into the deep ocean. To predict these transports, we must understand the turbulence that mixes the upper equatorial oceans.

While direct measurements of turbulence have been relatively sparse, other quantities that influence turbulence (e.g., wind stress) have been measured routinely for several decades. Much could be learned if we could reliably estimate turbulence properties based on those existing measurements. Here we use direct turbulence measurements to identify the environmental variables that are most predictive of turbulence amplitude and to calibrate and test turbulence parameterizations based on those routinely measured variables.

The turbulence measurements were made on the equator at 140°W, in the Pacific cold tongue. The Tropical Atmosphere and Ocean (TAO) mooring array (McPhaden 1995; McPhaden et al. 1998) has been deployed in the equatorial Pacific for several decades, measuring surface fluxes and subsurface temperature. Since 1990, the mooring at 140°W has also measured currents. Moored turbulence measurements at this location have been available since September 2005 (Perlin and Moum 2012; Warner and Moum 2019). Here we use those measurements to test and calibrate proxies for turbulence based on the surface fluxes and subsurface profiles of currents and temperature. We then use the proxies to extend the history of turbulence back through the 1990s.

In section 2, we review the physics of mixing in the Pacific cold tongue region, focusing on the deep cycle of equatorial turbulence. Section 3 describes the observations we employ. Statistical relationships between deep cycle turbulence and variables routinely measured on tropical moorings are described in section 4. This leads to two useful methods for parameterizing the turbulent kinetic energy dissipation rate, as described in section 5. Section 6 discusses uncertainties in these methods. As an example of the use of these parameterizations, we examine the annual mixing cycle in section 7. A discussion and summary is given in section 8.

2. The deep cycle of turbulence in the eastern Pacific cold tongue

Most of the ocean is capped by a surface mixed layer (ML), a layer of strong turbulence and uniform distributions of temperature T, salinity, and other properties extending for a few tens of meters beneath the surface. Directly below the ML, water properties are stratified and turbulence is generally much weaker. A well-known exception is found in the cold tongue region of the eastern equatorial Pacific, where the water below the ML is strongly turbulent despite stable thermal stratification. This combination can result in extraordinarily strong property exchanges with the ocean interior (Moum et al. 2009).

Turbulence in this stably stratified flow is made possible by the Equatorial Undercurrent (EUC), which flows eastward at $\sim 1\,\mathrm{m\,s^{-1}}$ at a depth of $\sim 100\,\mathrm{m}$. Above the EUC core, the current is sheared at a rate $\sim 10^{-2}\,\mathrm{s^{-1}}$, providing an energy source that can overcome the stable stratification and drive turbulence. This requires that the squared shear, $S^2 = (\partial U/\partial z)^2 + (\partial V/\partial z)^2$, exceed the squared buoyancy frequency $N^2 = \alpha_T g \partial T/\partial z$, by a factor of approximately 4. In the foregoing expressions, $\partial U/\partial z$ and $\partial V/\partial z$ represent vertical derivatives of the mean zonal and meridional currents,

Denotes content that is immediately available upon publication as open access.

Warner's current affiliation: Environmental Studies Program, Brandeis University, Waltham, Massachusetts.

Corresponding author: W. D. Smyth, bill.smyth@oregonstate.edu

DOI: 10.1175/JPO-D-20-0236.1

© 2021 American Meteorological Society. For information regarding reuse of this content and general copyright information, consult the AMS Copyright Policy (www.ametsoc.org/PUBSReuseLicenses).

Brought to you by OREGON STATE UNIVERSITY | Unauthenticated | Downloaded 01/31/22 08:20 PM UTC

respectively, α_T is thermal expansion coefficient and g is the gravitational acceleration.[1] Equivalently, we expect to encounter turbulence when the gradient Richardson number, $\mathrm{Ri} = N^2/S^2$, is less than a critical value near 1/4 (e.g., Smyth 2020).

A second contributor to shear above the EUC core is the South Equatorial Current (SEC). Driven by the trade winds, the SEC generally flows to the west, opposite to the EUC, thereby enhancing the shear and extending it toward the surface. During the Tropic Heat II cruise in 1987 (Moum et al. 1992), winds were variable and it was clear that turbulence between the ML base and the EUC core responds to wind changes on time scales of a few days. Turbulence was strongest when the wind was antiparallel to the EUC, the optimal direction for enhancing the shear.

Much of the time, the upper flank of the EUC is in a state of *marginal instability* (hereafter MI; Thorpe and Liu 2009), a quasi-equilibrium between the forcing of the shear by the trade winds, which reduces Ri, and turbulent mixing, which increases Ri. The result is that Ri fluctuates around the critical value ~1/4. An important property of MI turbulence is that it has two intrinsic time scales (S^{-1} and N^{-1}) but no intrinsic length scale, a challenge for parameterization. Moreover, the MI state is sensitive to small perturbations, making quantitative predictions doubly difficult. Recent descriptions of MI are provided in Smyth et al. (2019) and Smyth (2020).

The MI equilibrium state is often perturbed in the late afternoon when the daytime surface current spreads downward. The daytime surface current is propelled by the trade winds and is stabilized by solar radiation. That radiation is absorbed over the top few meters of the ocean, stratifying the water column and thereby allowing a strong shear to develop there (Price et al. 1986; Pham et al. 2017; Hughes et al. 2020). In the afternoon, this stabilizing effect is steadily reduced as the solar elevation decreases. A few hours before sunset, instability develops. No longer trapped at the surface, the current is entrained downward. Ultimately, it adds to the shear of the EUC, triggering enhanced turbulence that lasts from midevening until morning (Smyth et al. 2013; Pham et al. 2013).

Tied as it is to the diurnal cycle of the solar heat flux, this turbulence regime is called the ''deep cycle'' (hereafter DC; Gregg et al. 1985; Moum and Caldwell 1985; Lien et al. 1995). DC turbulence is found in a layer that extends vertically from the base of the surface ML to just above the EUC core, called the deep cycle layer (DCL). Our goal is to parameterize turbulence properties averaged over this layer.

Most previous attempts to parameterize equatorial turbulence have been based on nondimensional functions of Ri alone, with dimensions supplied by a multiplicative constant (Pacanowski and Philander 1981; Peters et al. 1988; Large et al. 1994). We know, however, that turbulence in the presence of a given Ri can take a wide range of amplitudes (Peters et al. 1988; Moum et al. 1989; Smyth 2020), and therefore that the Ri-dependent parameterizations are not generally valid. Zaron and Moum (2009) addressed this problem using dimensional reasoning much as we do here, but the result depended on variables that are not Galilean invariant and therefore cannot be generally valid. Here, we confine our attention to Galilean-invariant variables. We also focus exclusively on turbulence in the deep cycle.

Using a simple layer model, Smyth et al. (2017) suggested a nocturnal mean value of dissipation in the deep cycle:

$$\varepsilon = \frac{\boldsymbol{\tau} \cdot \mathbf{S}}{\rho_0}, \tag{1}$$

where ρ_0 is a characteristic water density. The full vector forms of wind stress $\boldsymbol{\tau} = \{\tau_x, \tau_y\}$ and shear $\mathbf{S} = \{\partial U/\partial z, \partial V/\partial z\}$ are included as a dot product since the component of wind stress aligned with the shear is the most effective at generating unstable shear and thus turbulence. Here, we set aside the modeling assumptions of Smyth et al. (2017) and instead test a wide range of variables for correlation with deep cycle turbulence averaged over the full diurnal cycle.

3. Observations

The dataset we use here is both intrinsically interesting and extensive enough to support statistical parameterization testing. The parameterizations are chosen with a view to potential uses with other datasets. The surface stress and heat flux (both solar and total) are obtained from the TropFlux reanalysis dataset (Praveen Kumar et al. 2013) and are daily averages at four points located 0.5° from 0°, 140°W. Subsurface data, including profiles of T, U, and V, are daily averages from the TAO mooring at 0°, 140°W (McPhaden 1995; McPhaden et al. 1998).

Currents are measured via a surface-mounted acoustic Doppler current profiler and are reliable only below about 30 m depth. When current speeds are needed at shallower depths, they are inferred using the surface wind stress and the surface mixed layer depth together with near-surface current meters following the method of Pham et al. (2017).

Since September 2005, the TAO mooring at 0°, 140°W has been supplemented by deployments of χpods, which use fast-response thermistors to collect thermal microstructure data at nominal depths between 29 and 119 m, from which the temperature variance dissipation rate χ_T is inferred (Moum and Nash 2009). Data are stored as 10-min averages. Along with the vertical temperature derivative T_z, χ_T is input to the formulas of Osborn and Cox (1972) and Osborn (1980) to obtain an estimate of the turbulent kinetic energy dissipation rate, ε_χ (Moum and Nash 2009; Perlin and Moum 2012; Warner and Moum 2019).

For this study, the χpod results are binned into daily averages to match the TAO and TropFlux data. Statistically, the dissipation rate is dominated by rare, powerful events, even at this level of averaging (Fig. 1). Gaps in the χpod record are due to problems with the mooring (also reflected in the ML, MI, and EUC records) or with the instrument itself.

The dissipation rate is also averaged vertically over the DCL. Following Pham et al. (2017), the deepest extent of the

[1] Saline stratification is weak in this region and is sparsely measured, so we neglect it for this discussion; for further details, see Pham et al. (2017).

Brought to you by OREGON STATE UNIVERSITY | Unauthenticated | Downloaded 01/31/22 08:20 PM UTC

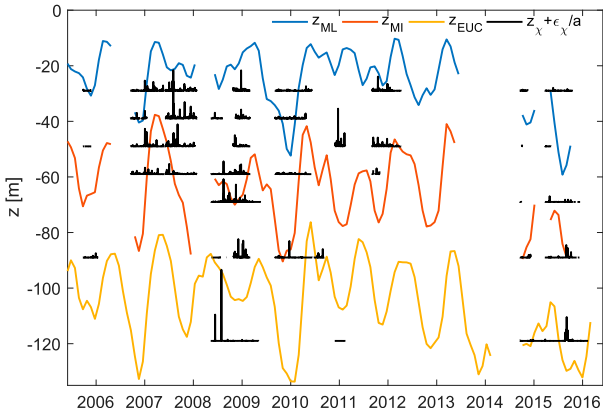

FIG. 1. Black lines indicate χpod nominal depths and daily averaged dissipation rate, combined as $z_\chi + \varepsilon_\chi/a$, where the scaling constant $a = 2 \times 10^{-6}\,\mathrm{m\,s^{-3}}$. Colored curves indicate the DML, MI, and EUC depths as specified in the legend. Depths are monthly averages smoothed with a binomial filter for clarity.

ML on a given day is defined approximately by a temperature drop of 0.16 K from the surface temperature. The base of the deep cycle is identified as the deepest level where Ri $< 1/4$ (e.g., Lien et al. 1995). See appendix A for further details.

4. Which variables govern the deep cycle?

Parameterization of turbulence statistics is a challenge of long standing. Our goal here is to predict average values of ε_χ, the turbulent kinetic energy dissipation rate detected by χpod, within the DCL, on the basis of daily-averaged data recorded at the TAO mooring array, specifically surface fluxes and current and temperature profiles.

The present understanding of DC physics suggests that the turbulence is governed primarily by its two principal energy sources, 1) the vertical shear of the horizontal mean currents **S** in the DCL, and 2) the wind stress $\boldsymbol{\tau}$. The shear provides the proximate energy source for turbulence. The wind plays a dual role: it is the original energy source for the SEC and the EUC, and it drives the daytime surface current that triggers strong turbulence each evening (section 2).

We assume that the dissipation rate characteristic of deep cycle turbulence, i.e., the average of ε over the deep cycle layer and over a time period of one day or longer, depends on the following primary governing variables:

- The friction velocity $u_* = \sqrt{\tau/\rho_0}$, or its vector counterpart $\boldsymbol{\tau}/\rho_0$.
- The shear in the deep cycle **S.**
- J_b^{sw} is the solar buoyancy flux. This could be replaced by the net flux J_b^{net}, but J_b^{sw} has the advantages of being single-signed and of representing the diurnal variation of the buoyancy flux; an important influence on the deep cycle (section 2).
- $h_{\mathrm{ML}} = -z_{\mathrm{ML}}$ is the nocturnal maximum thickness of the surface mixed layer (appendix A). Other potentially important length scales include $h_{\mathrm{DCL}} = z_{\mathrm{ML}} - z_{\mathrm{MI}}$, the thickness of the DCL, and $h_{\mathrm{EUC}} = -z_{\mathrm{EUC}}$, the depth of the EUC core.

All quantities are daily averages, and depth-dependent variables are also averaged over the DCL.

From ε and its main governing variables u_*, **S**, J_b^{sw}, and h_{ML}, Buckingham's Pi theorem (Kundu et al. 2016) guarantees that we can construct exactly three independent dimensionless combinations. We choose these to be

$$\Pi_1 = \frac{\varepsilon}{|J_b^{\mathrm{sw}}|}; \quad \Pi_2 = \frac{Su_*^2}{|J_b^{\mathrm{sw}}|}; \quad \Pi_3 = \frac{u_*^3}{h_{\mathrm{ML}} J_b^{\mathrm{sw}}}. \tag{2}$$

The combination Su_*^2 may usefully be replaced by the vector dot product $\mathbf{S} \cdot \boldsymbol{\tau}/\rho$, isolating the parallel components of wind and shear.

This limited selection of governing variables is easily expanded. To include a dependency on N, the buoyancy frequency in the deep-cycle layer, we add a fourth nondimensional combination

$$\Pi_4 = \frac{N^2}{S^2} = \mathrm{Ri} \tag{3}$$

and, optionally, replace S by N in the definition of Π_2. Similarly, if we think nocturnal surface cooling is important (perhaps because convective plumes in the ML can trigger turbulence in the DCL), we can add the mean nocturnal buoyancy flux $J_b^{\mathrm{cool}} = J_b^{\mathrm{net}} - J_b^{\mathrm{sw}}$ via

$$\Pi_5 = -\frac{J_b^{\mathrm{cool}}}{J_b^{\mathrm{sw}}} \tag{4}$$

and, optionally, replace J_b^{sw} with J_b^{cool} in the other nondimensional combinations. The other relevant length scales, $h_{\mathrm{DCL}} = z_{\mathrm{ML}} - z_{\mathrm{MI}}$ and z_{EUC} are incorporated by adding

$$\Pi_6 = -\frac{z_{\mathrm{EUC}}}{h_{\mathrm{ML}}}; \quad \Pi_7 = -\frac{h_{\mathrm{DCL}}}{z_{\mathrm{ML}}}, \tag{5}$$

and, optionally, replacing h_{ML} in Π_3. The same can be done with the individual components of the wind stress $\{\tau_x, \tau_y\}$ and the shear $\{S_x, S_y\} = \{\partial U/\partial z, \partial V/\partial z\}$ can be included in the same way.

Figure 2 shows all of these candidate governing variables as 30-day averages. In many of the variables, the dominant fluctuation is annual, but J_b^{sw} is primarily semiannual as the sun crosses the equator twice a year. Several variables show disruptions associated with the super–El Niño events of 1997/98 and 2015/16. In what follows, we will use statistical methods to extract the relationships of the variables, and their nondimensional combinations, with ε_χ.

The Spearman rank correlation coefficient R_S indicates the relative likelihood of a functional relationship between two variables, assuming that the relationship is one-to-one but not necessarily linear (Press et al. 1992). First, we test the rank correlation of each potential governing variable with ε_χ (Fig. 3). The correlation is also illustrated using bin medians of the daily values. The correlation is largest for wind stress (Figs. 3a–c), specifically the zonal component (Fig. 3b), for which $R_s = 0.43$.

A weaker correlation exists between ε_χ and shear (Figs. 3d–f), mainly its zonal component S_x. The correlation with N^2 is smaller (Fig. 3g) and those with the solar and net buoyancy

Brought to you by OREGON STATE UNIVERSITY | Unauthenticated | Downloaded 01/31/22 08:20 PM UTC

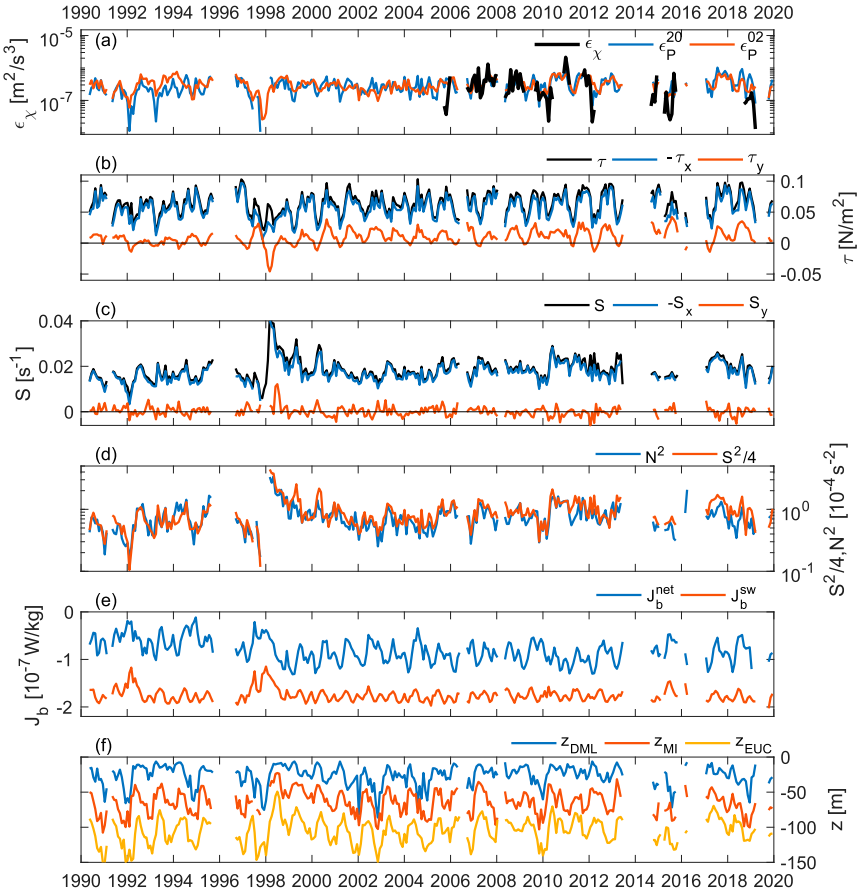

FIG. 2. (a) Turbulent kinetic energy dissipation rate as measured by χpod (black) and by two proxies [(7) and (8)]. (b) Wind stress and components as shown in legend, (c) shear and components, (d) squared buoyancy frequency (blue) and squared shear magnitude (red), scaled so that equality indicates Ri = 1/4, (e) solar (red) and net (blue) surface buoyancy flux, and (f) mixed layer base (red) and EUC core (blue). Subsurface variables are averaged over the DCL. All variables are shown as 30-day averages for clarity. Note that the signs of τ_x in (b) and S_x in (c) are reversed.

fluxes are smaller still (Figs. 3h,i). Among the length scales, the correlations with ε_χ are all small. We retain the choice of the diurnal mixed layer thickness h_{ML} (Fig. 3k) as our length scale, not because it influences ε_χ but because it can be measured when velocity data are not available.

We therefore expect that the nondimensional combinations involving wind stress and shear identified in (2) will capture most of the variability. This is confirmed by examining the rank correlations among the Π values themselves (Fig. 4). As suggested above, Su_*^2 has been replaced by $\mathbf{S}\cdot\boldsymbol{\tau}/\rho_0$ in the definition of Π_2. We therefore expect that Π_2 and Π_3 (Figs. 4a,b), whose rank correlations with Π_1 are much greater than those of Π_4–Π_7 (Figs. 4c–f), will have the best predictive capacity.

5. Predicting the deep cycle

Guided by the above results, we consider approximations of the general form

$$\varepsilon_P^{\alpha\beta} = A_{\alpha,\beta}|J_b^{\mathrm{sw}}|\left(\frac{\mathbf{S}\cdot\boldsymbol{\tau}}{\rho_0|J_b^{\mathrm{sw}}|}\right)^{\alpha}\left(\frac{u_*^3}{h_{\mathrm{ML}}|J_b^{\mathrm{sw}}|}\right)^{\beta}. \tag{6}$$

The multiplicative factor $A_{\alpha,\beta}$ is chosen such that the arithmetic means of $\varepsilon_P^{\alpha\beta}$ and ε_χ (over days when both values are available) are equal. The exponents α and β will be determined next.

The simplest cases of (6) involve only Π_2 or only Π_3, i.e., either $\alpha = 0$ or $\beta = 0$. If both exponents are nonzero, the approximation requires more measurements, but it has the potential to be more accurate. In this case, that turns out not to be true; no combination of nonzero α and β makes a better approximation than the simpler cases with $\alpha = 0$ or $\beta = 0$ (see details in the appendix B). We therefore focus on the latter.

Small values of the exponent lead to a relatively conservative approximation. The proxy fails to match the largest and smallest values of ε_χ, but errors are limited. In contrast, a large exponent promotes large variations, which capture extreme events but are also prone to large errors.

Brought to you by OREGON STATE UNIVERSITY | Unauthenticated | Downloaded 01/31/22 08:20 PM UTC

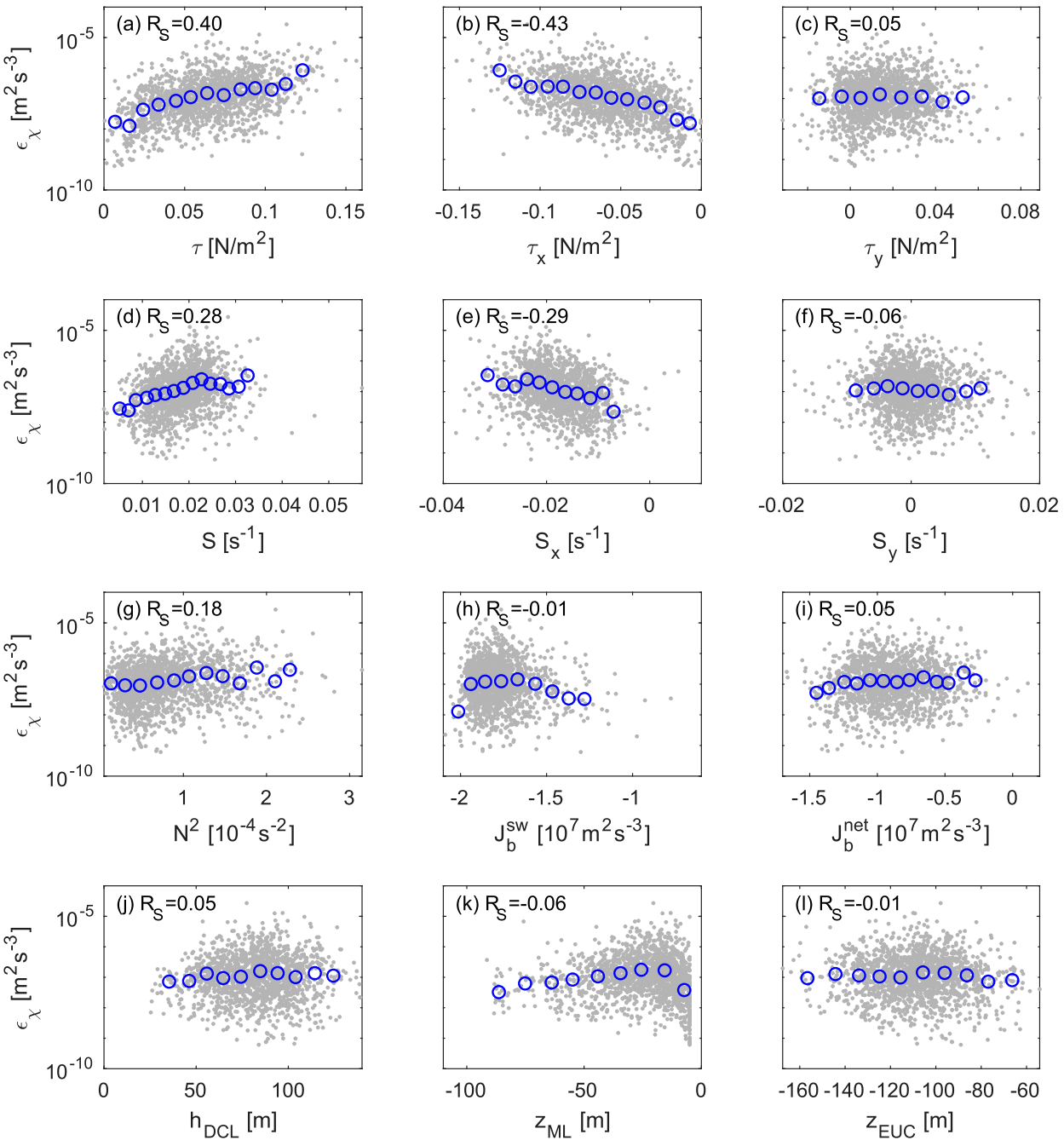

FIG. 3. Scatterplots of ε_χ vs potential governing variables. Gray dots represent daily values. Blue circles are the median values in evenly spaced bins of the abscissa. Annotations indicate the Spearman rank coefficient R_S.

We therefore examine cases where only one exponent is nonzero and seek values for that exponent that are neither too large nor too small. After careful examination (appendix B), we identify two cases that merit further testing: $\{\alpha, \beta\} = \{2, 0\}$ and $\{0, 2\}$, i.e.,

$$\varepsilon_P^{20} = A_{20}|J_b^{\mathrm{sw}}|\left(\frac{\mathbf{S}\cdot\boldsymbol{\tau}}{\rho_0 J_b^{\mathrm{sw}}}\right)^2; \quad A_{20} = 0.0414 \tag{7}$$

and

$$\varepsilon_P^{02} = A_{02}|J_b^{\mathrm{sw}}|\left(\frac{u_*^3}{h_{\mathrm{ML}} J_b^{\mathrm{sw}}}\right)^2; \quad A_{02} = 73.9. \tag{8}$$

The latter version has the advantage of being usable without the need for current measurements. Specifically, it requires only wind stress, solar buoyancy flux, and ocean density profiles

Brought to you by OREGON STATE UNIVERSITY | Unauthenticated | Downloaded 01/31/22 08:20 PM UTC

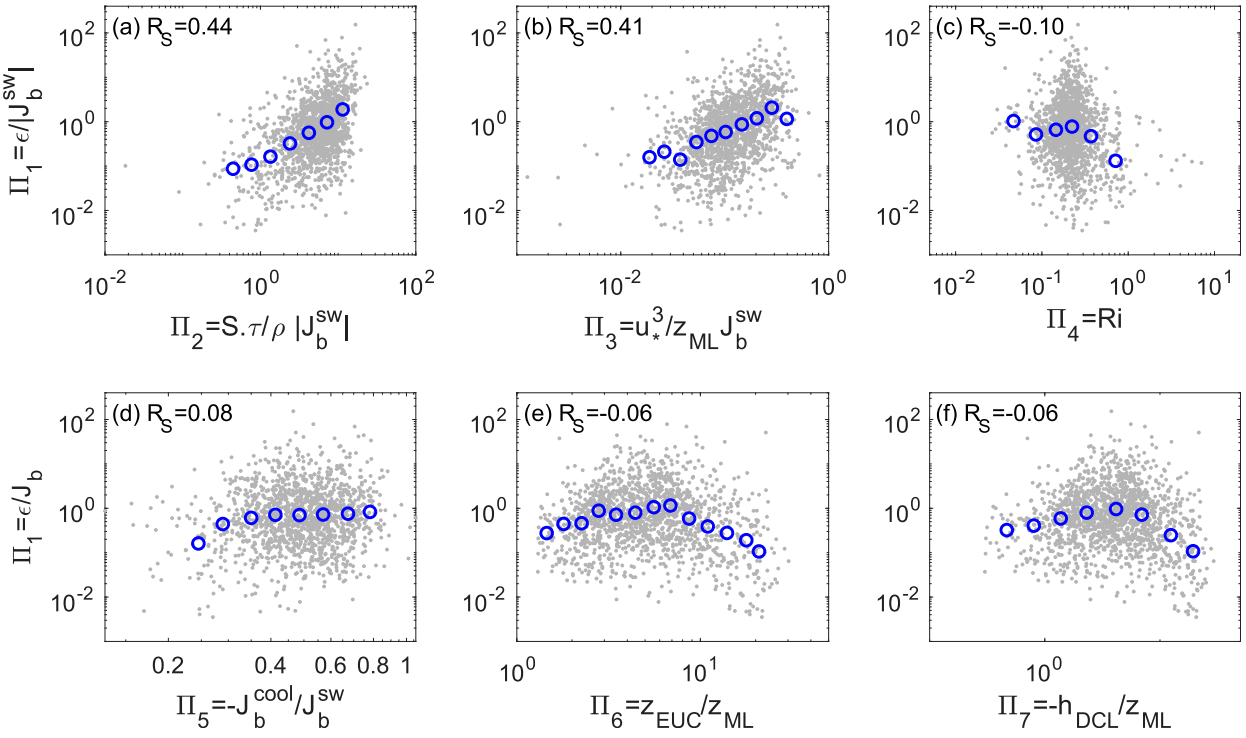

FIG. 4. Scatterplots of Π_1 vs (a)–(f) Π_2– Π_7, respectively. Gray dots represent daily values. Blue circles are the median values in log-spaced bins of the abscissa. Annotations indicate the Spearman rank coefficient R_S.

that resolve the mixed layer. This greatly expands its applicability to historical mooring data, which only occasionally includes well-resolved current profiles.

6. Sources of uncertainty

For both (7) and (8), there is a visible correlation between the daily-averaged measured values and the proxy, albeit with significant scatter (Figs. 5a,b). The 15-day averaged data maintain the correlation but show less scatter. [The 15-day period is chosen to facilitate comparison with Perlin and Moum (2012), see below.] In quantitative terms, the Pearson linear correlation coefficients for daily and 15-day values are 0.28 and 0.57 for (7) and 0.14 and 0.46 for (8), respectively.

A rough relative error estimate, valid for 67% of values for both (7) and (8), is a factor of 6 for daily averages and a factor of 3 for estimates averaged over 15 days. (These were arrived at by sorting the error values shown in Figs. 5c,d.) Averaged over longer times, the proxies become more reliable, as will be illustrated in section 7. Several factors could account for this level of uncertainty.

- We could be neglecting some factors that influence the deep cycle. For example, no account is taken of the detailed form of the velocity and temperature profiles, nor of any potential effect of salinity gradients.
- There is arbitrariness in our definition of the layer over which deep cycle physics is active.
- The algebraic form (6) of the proxies considered is only a subset of the infinite range of functional forms allowed by Buckingham's theorem.
- We have assumed that deep cycle turbulence is local in time, i.e., that the turbulence in a given time period is fully determined by environmental conditions within that same period. In fact, history effects are likely to be important, especially on short-term (e.g., daily) averages. For example, the parameterization (8), which excludes the direct influence of shear, may err due to shear changes that originate in wind shifts but are communicated to the EUC over many months by equatorial waves.
- The χpods and the TAO sensors are spaced differently in the vertical. This could affect the resulting values of ε differently under different conditions.
- Uncertainty in the χpod measurements themselves is a factor. Comparison between estimates of ε from χpod and from a microstructure profiler at the same depth, averaged over 15 days, agree to within a factor of 2 in 12 cases out of 17 (Perlin and Moum 2012, their Fig. 5), comparable to the factor of 3 uncertainty found here.

7. Application: Seasonal variation of deep cycle turbulence

We next apply (7) and (8) to the seasonal variation of the deep cycle. This includes the annual cycle as well as its shorter-period (e.g., semiannual) harmonics. It is well established that turbulence in the deep cycle decreases to a minimum in boreal spring (Moum et al. 2013). Observations (Moum et al. 2013; Liu et al. 2016) and large-eddy simulations (Pham et al. 2017) have also hinted at a second minimum in boreal fall, though

Brought to you by OREGON STATE UNIVERSITY | Unauthenticated | Downloaded 01/31/22 08:20 PM UTC

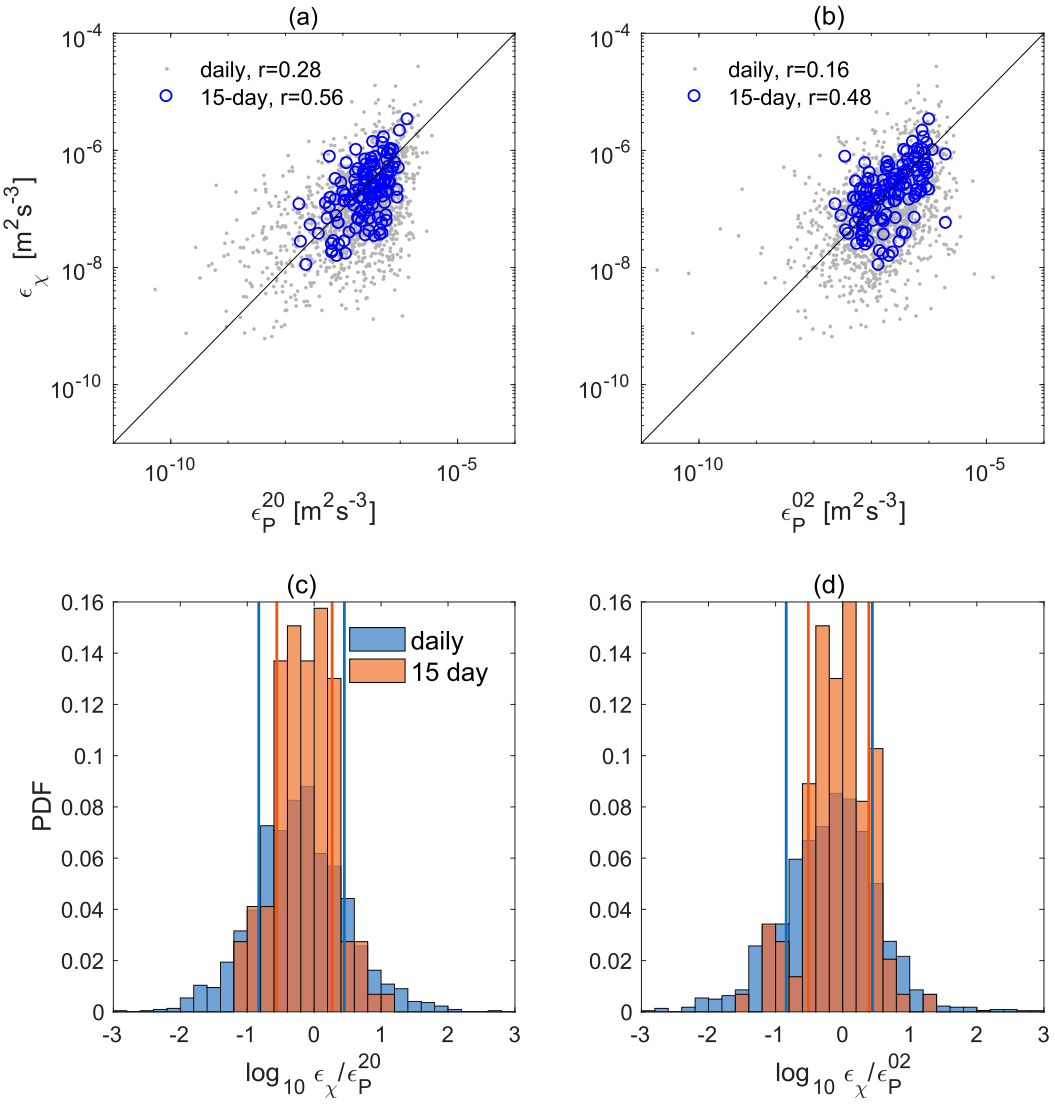

FIG. 5. Comparison of measured vs proxy values of ε: (left) ε_P^{20} and (right) ε_P^{02}. (a),(b) Gray dots and blue circles represent daily values and 15-day averages, respectively. Annotations show the linear correlation coefficient. (c),(d) Probability distribution functions for the ratio of measured/proxy dissipation rates. Vertical lines show the first and fifth sextiles.

that feature has not been examined explicitly. Using the additional observational data now available, together with the proxies (7) and (8), we can confirm that the second minimum exists (Fig. 6a,b, black curve) and consider its causes.

The semiannual variation of the deep cycle is evident in ε_χ and in both proxies (7) and (8). The fall minimum is both shorter and less pronounced than the springtime minimum. If we include only the subset of days for which ε_χ and the proxies are all available (Fig. 6a), the confidence limits on the means of ε_P^{20} and ε_P^{02} are comparable to those of ε_χ. Agreement is adequate except in the month of May, when ε_P^{02} exceeds ε_χ by a factor of 5. This is due to an episode of unusually shallow ML in May 2010 (appendix B, Fig. B2).

When the entire interval 1990–2020 is included (Fig. 6b), the confidence limits on the proxies are thin compared with the observations because (7) and (8) are applied to a much longer data period. Specifically, the number of days included in the monthly averages of ε_χ range from 93 (August) to 231 (December). For the proxy (7), the corresponding number of days is 804–848, and for (8), 726–877. With this longer time series, the anomalously high value in May is largely removed.

The amplitude of the seasonal cycle is noticeably smaller in the proxy estimates, and in ε_P^{20} the August maximum is shifted to July. These remaining discrepancies could indicate a flaw in the proxies, but they could also reveal a genuine difference in mixing between the time periods when the different instruments were deployed. Specifically, the seasonal mixing cycle may have been relatively weak in the 1990s, perhaps linked with the positive phase of the interdecadal Pacific oscillation (England et al. 2014).

Brought to you by OREGON STATE UNIVERSITY | Unauthenticated | Downloaded 01/31/22 08:20 PM UTC

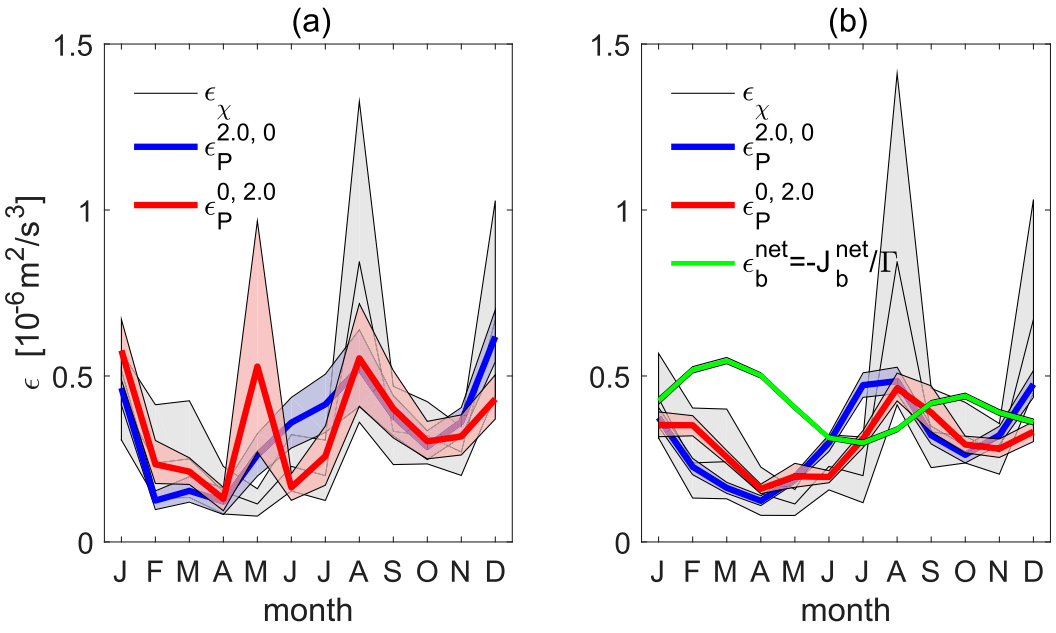

FIG. 6. Measured and parameterized dissipation rates binned as monthly means. Gray shading shows the 95% bootstrap confidence limits on the mean for each month. (a) Only days where both ε_χ and the proxies are available. (b) All days. The green curve in (b) shows the net surface buoyancy flux scaled for comparison with the dissipation rates.

The fall minimum in DC turbulence is associated with a slackening of the trade winds (Fig. 7b) which coincides with a reduction of the shear in the DCL (Fig. 7c). The product of these two vector quantities dominates the proxy ε_P^{20}, defined in (7). That product shows a distinct minimum in October (Fig. 7d). A secondary factor is a slight increase of solar heating (Fig. 7e), which appears in the denominator of ε_P^{20}. The proxy ε_P^{02}, defined in (8), does not involve the shear directly, and its dependence on the ML thickness has little influence. Instead, ε_P^{02} is governed almost entirely by wind stress, whose decrease in boreal fall is modest (Fig. 7b). Despite this, ε_P^{02} successfully reproduces the fall minimum in ε_χ because the wind stress appears cubed in (8).

In summary, the semiannual variation of the deep cycle is mainly accounted for by changes in the wind stress. The direct effect of solar heating is small, though it likely plays a role in driving the wind stress variation.

It is interesting to compare these turbulence dissipation rate estimates with the surface buoyancy flux by rearranging the formula of Osborn (1980) for the turbulent buoyancy flux: $\varepsilon_b^{\text{net}} = -J_b^{\text{net}}/\Gamma$, with $\Gamma = 0.2$ (Smyth 2020). The equivalent dissipation rate $\varepsilon_b^{\text{net}}$ (Fig. 6b, green curve) is the turbulent dissipation rate that would be required to carry the net surface buoyancy flux exactly. The net surface buoyancy flux has the effect of warming the ocean in all months. It does so most strongly in March and least strongly in July.

In these terms, the turbulence is approximately out of phase with the surface buoyancy flux, i.e., it is weak when surface warming is strong, and vice versa. The difference between $\varepsilon_b^{\text{net}}$ and the deep cycle dissipation rate is a measure of the net warming of the ML. This warming is partly reflected in actual temperature change and partly balanced by horizontal advection, which generally carries ML heat toward the western Pacific warm pool (McPhaden and Picaut 1990).

Moum et al. (2013) performed a similar analysis, focusing on the sea surface temperature and using a smaller dataset than we have today. Consistent with Moum et al. (2013), Fig. 6b suggests strong warming of the ML in boreal winter and spring. We find that the warming period lasts one month longer than in the earlier Moum et al. result: from February to June inclusive. In July and August, DC turbulence removes heat from the ML faster than the sun can replenish it, leading to a net cooling. Both proxies indicate that this summertime cooling is less dramatic than is suggested by the χpod measurements. This may be because, even now, the χpods have been operational over only three realizations of the month of August (2007, 2008, and 2015) and those Augusts may have been unusually turbulent relative to the longer period of 1990–2020.

8. Summary and discussion

We have explored methods for extracting information about equatorial deep cycle turbulence from historical mooring records that extend long before turbulence measurements were regularly included. Using χpod measurements made on the equator at 140°W since September 2005 as our "ground truth," we have derived (7) and (8), two functional combinations of wind stress, current shear, solar heat flux and mixed layer thickness that can be used to infer the turbulent kinetic energy dissipation rate in the equatorial deep cycle. The proxies are applied to daily-averaged data, then the results are averaged over longer times to reduce random discrepancies. For daily

Brought to you by OREGON STATE UNIVERSITY | Unauthenticated | Downloaded 01/31/22 08:20 PM UTC

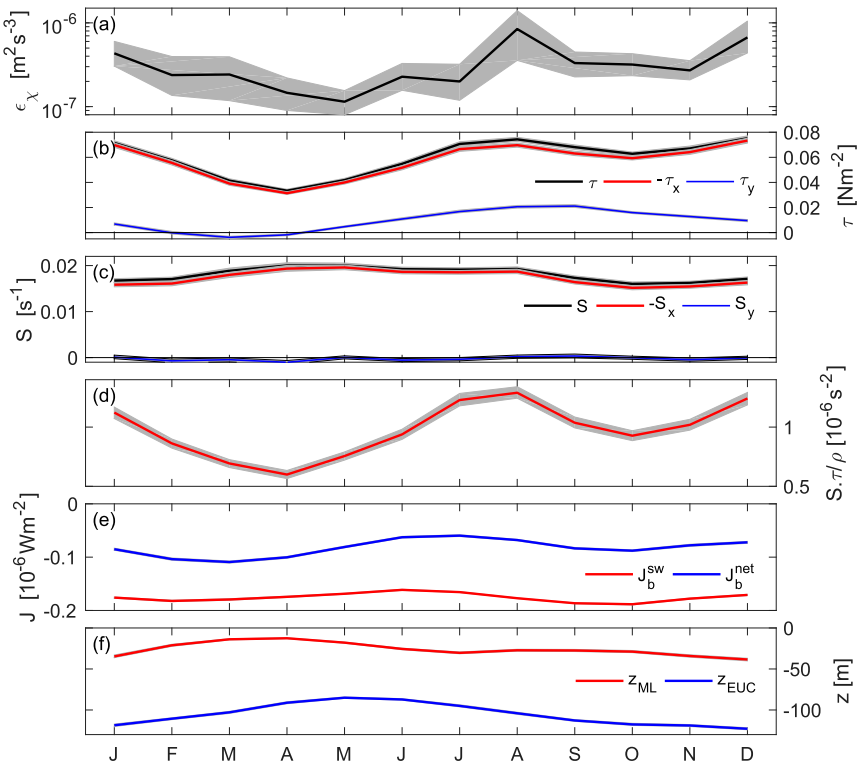

FIG. 7. (a) Monthly averages of ε_χ and variables involved in the proxies (7) and (8). (b) Wind stress and its westward and northward components. (c) Shear and its westward and northward components. (d) Dot product of shear and scaled wind stress. (e) Locations of ML base and EUC core. (f) Shortwave and net surface buoyancy fluxes. Shaded areas indicate 95% confidence limits on the mean. In (e) and (f) these are too small to be visible.

averages, a typical discrepancy between the proxies and ε_χ is a factor of 6, whereas for 15-day averages the difference is reduced to a factor of 3 (comparable to the uncertainty in ε_χ itself).

The proxies discussed here are based on basic variables like wind stress and shear, rather than more complex constructs that would isolate tropical instability waves (TIWs) and other specific sub- and mesoscale phenomena. Future versions might include variables such as the kinetic energy associated with TIWs (e.g., Liu et al. 2016), and might thereby make improved predictions of turbulence. The proxies are based on the known physics of the equatorial deep cycle. Adaptations for more general turbulent flow regimes remain to be explored.

The proxies have been applied to 28 years of mooring data to refine our understanding of the seasonal mixing cycle in the eastern Pacific cold tongue. In addition to the previously identified minimum in boreal spring, there is a second minimum in boreal fall, with intervening maxima in December and July–August. The maximum dissipation rates exceed the minima by a factor of 4. The proximate cause of the fall minimum is a slight slackening of the trade winds, to which the turbulent dissipation rate is highly sensitive.

In an upcoming study we will use the same techniques to explore variations in the deep cycle related to El Niño–Southern Oscillation, extending the results of Warner and Moum (2019). These techniques will also be applied to other near-equatorial moorings where direct turbulence measurements are not available in order to gauge the areal extent of deep cycle turbulence and thus assess its impact on the global climate.

Acknowledgments. TAO mooring data were acquired from web archives provided by the TAO Project Office of NOAA/PMEL: https://www.pmel.noaa.gov/tao/drupal/disdel/. The TropFlux data, accessed at https://incois.gov.in/tropflux, is produced under a collaboration between Laboratoire d'Océanographie: Expérimentation et Approches Numériques (LOCEAN) from Institut Pierre Simon Laplace (IPSL, Paris, France) and National Institute of Oceanography/CSIR (NIO, Goa, India), and supported by Institut de Recherche pour le Développement (IRD, France). TropFlux relies on data provided by the ECMWF Re-Analysis interim (ERA-I) and ISCCP projects. This work was supported by the U.S. National Science Foundation under Grants OCE-1256620, OCE-1431518, OCE-1355768, and OCE-1851520.

Data availability statement. TAO mooring data were acquired from web archives provided by the TAO Project Office of NOAA/PMEL: https://www.pmel.noaa.gov/tao/drupal/disdel/. The TropFlux data were accessed at https://incois.gov.in/tropflux. The global mean SAT is available at https://www.ncdc.noaa.gov/

Brought to you by OREGON STATE UNIVERSITY | Unauthenticated | Downloaded 01/31/22 08:20 PM UTC

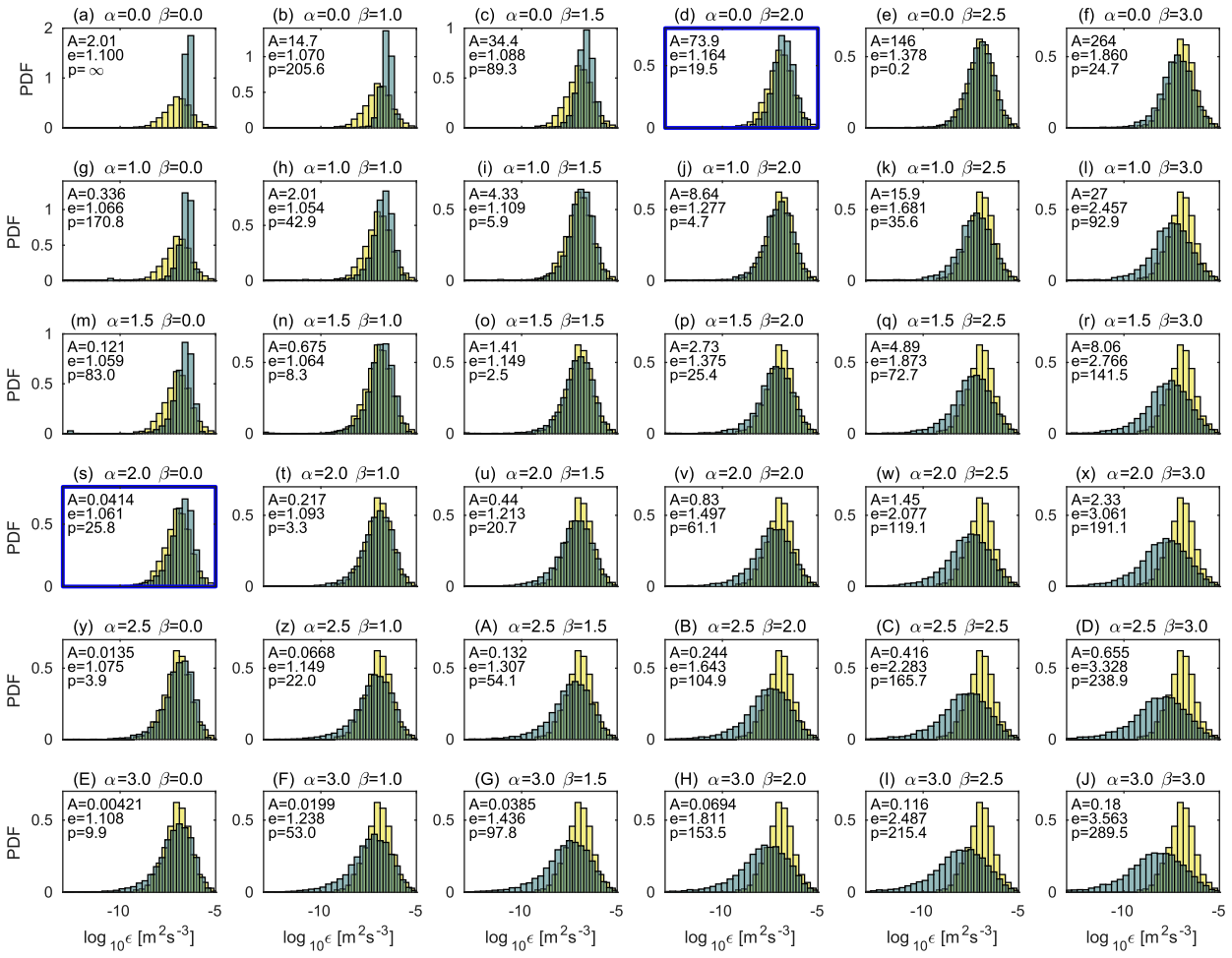

FIG. B1. Probability distribution functions of the dissipation rate (ε_χ, light bars) and the proxy ($\varepsilon_P^{\alpha\beta}$, dark bars). In each frame, A represents the coefficient $A_{\alpha\beta}$ in the general proxy Eq. (6). The error parameter e is the root-mean-square difference between daily averages of ε_χ and $\varepsilon_P^{\alpha\beta}$, divided by $10^{-6}\,\mathrm{m^2\,s^{-3}}$. The parameter p, computed as minus the logarithm of the output of the Kolmogorov–Smirnov test (Press et al. 1992) applied to ε_χ and $\varepsilon_P^{\alpha\beta}$, is small if the PDFs are similar. Blue borders highlight the cases chosen for further analysis.

cag/global/time-series, and the ONI is at https://psl.noaa.gov/data/correlation/oni.data. Processed data are available upon request from W. Smyth and J. Moum.

APPENDIX A

Bounding the Deep Cycle Layer

The DCL is bounded above by the base of the ML and from below by the shallowest depth below which Ri > 0.25. The ML base is identified as the shallowest depth at which $T = T_0 - 0.16°\mathrm{C}$, T_0 being the shallowest temperature measured. This criterion was shown by Pham et al. (2017) to approximate the deepest nocturnal extent of the diurnally varying ML based on daily averaged temperature profiles.

The base of the DCL is the shallowest depth at which Ri, computed from daily averaged temperature and velocity, is equal to or less than 0.25. Although averaging the velocity profile often leads to an overestimate of Ri (which would suggest that the critical value Ri = 0.25 be replaced by some arbitrary higher value), in this case the shear is dominated by the EUC, which varies little in the course of a day, and Ri is therefore adequately resolved in daily-averaged data (Pham et al. 2017, appendix A).

Daily averaged temperature and velocity profiles are interpolated onto a 5 m vertical grid using cubic splines and their derivatives are computed as second-order centered differences. The depths satisfying the criteria for the bases of the ML and the DCL are found via linear interpolation between neighboring grid points.

APPENDIX B

Optimal Values for α and β

We seek optimal values for the exponents α and β in (6). We begin by comparing ε_χ with $\varepsilon_P^{\alpha\beta}$, computed using example values $\alpha, \beta = 0, 1, 1.5, 2, 2.5, 3$. We compare both probability distribution functions (PDFs) and estimates of the root-mean-square error (Fig. B1). If the proxy were perfect, the

Brought to you by OREGON STATE UNIVERSITY | Unauthenticated | Downloaded 01/31/22 08:20 PM UTC

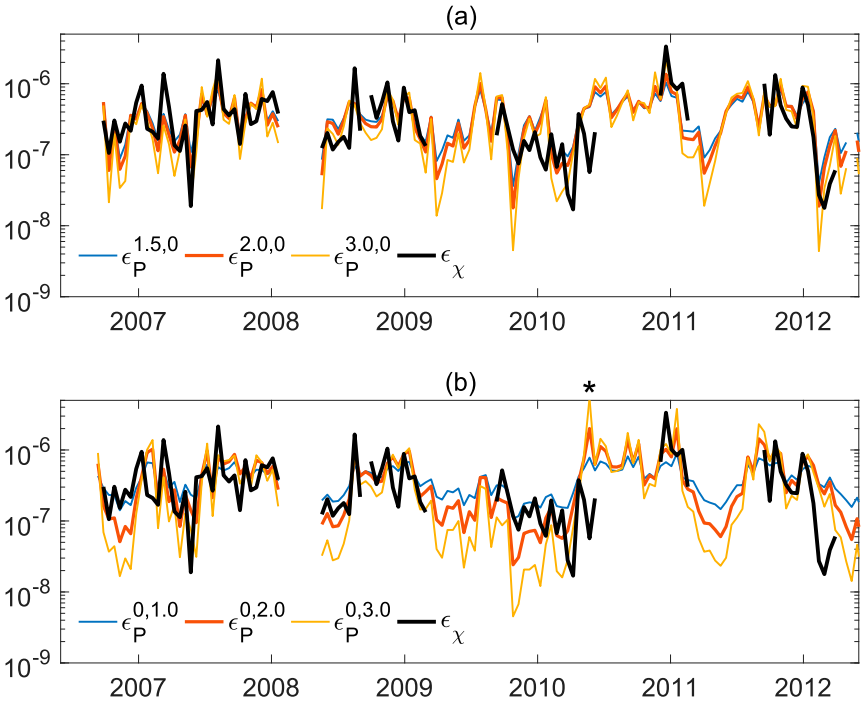

FIG. B2. Illustrative sample of the time series $\varepsilon_\chi(t)$ (black) and the proxies with (a) $\beta = 0$ and (b) $\alpha = 0$ as labeled. In each case the thick red curve shows the preferred proxy. Data are binned into 15-day intervals for clarity. The asterisk above (b) highlights a particular discrepancy discussed in the text.

distributions would be identical and the error estimate would be zero.

First consider the case $\beta = 0$. Sample results for $\alpha = 0, 1, 1.5, 2, 2.5$, and 3 appear in the leftmost column of Fig. B1. The root-mean-square error, scaled by $10^{-6}\,\mathrm{m^2\,s^{-3}}$, is labeled e. This measure of error is smallest when $\alpha = 1.5$ and $e = 1.059$. In this case, the distribution of the proxy ε_p (dark bars) is much thinner than that of ε_χ (light bars), i.e., the approximation is relatively conservative in consequence of the smallness of α. Increasing α to 2.0 gives only a slight increase in the error ($e = 1.061$) but better agreement in the width of the pdf. Increasing in α further to 2.5 improves the pdf at the cost of a more significant increase in e. We therefore select the case $\alpha = 2, \beta = 0$ for further consideration.

When $\alpha = 0$ (top row in Fig. B1), the smallest error is obtained by setting $\beta = 1$, but once again this is an overly conservative approximation. The best match in the pdf is found when $\beta = 2.5$, but at the cost of increased e. As a compromise value, we select $\beta = 2$, which gives $e = 1.164$.

Cases in which both α and β are nonzero are generally less promising. They have the practical disadvantage of requiring measurements of both the shear and the ML thickness. An example of these is the case $\{\alpha, \beta\} = \{1.5, 1\}$. Though it does well in terms of our error metrics e and p, we find in practice that the improvement is negligible and the added complication is therefore not justified.

In summary, we identify two cases: $\{\alpha, \beta\} = \{2, 0\}$ and $\{0, 2\}$, for further testing. When these are compared with the time series of ε_χ (Fig. B2) the match is generally good, though occasional large discrepancies are evident. The effects of different $\{\alpha, \beta\}$ are also visible. In most cases the discrepancies involve very low dissipation rates that contribute little to longer-term averages. However, in May 2010, the ML was unusually shallow, causing (8) to overestimate ε_χ by nearly two orders of magnitude (asterisk above Fig. B2b). The implications of this are discussed in the main text.

REFERENCES

England, M., and Coauthors, 2014: Recent intensification of wind-driven circulation in the Pacific and the ongoing warming hiatus. *Nat. Climate Change*, **4**, 222–227, https://doi.org/10.1038/nclimate2106.

Gregg, M., H. Peters, J. Wesson, N. Oakey, and T. Shay, 1985: Intensive measurements of turbulence and shear in the equatorial undercurrent. *Nature*, **318**, 140–144, https://doi.org/10.1038/318140a0.

Hughes, K. G., J. N. Moum, and E. L. Shroyer, 2020: Heat transport through diurnal warm layers. *J. Phys. Oceanogr.*, **50**, 2885–2905, https://doi.org/10.1175/JPO-D-20-0079.1.

Kundu, P., I. Cohen, and D. Dowling, 2016: *Fluid Mechanics.* 6th ed. Academic Press, 952 pp.

Large, W., J. McWilliams, and S. Doney, 1994: Ocean vertical mixing: A review and a model with a nonlocal boundary layer parameterization. *Rev. Geophys.*, **32**, 363–403, https://doi.org/10.1029/94RG01872.

Lien, R.-C., D. Caldwell, M. Gregg, and J. Moum, 1995: Turbulence variability at the equator in the central Pacific at the beginning of

Brought to you by OREGON STATE UNIVERSITY | Unauthenticated | Downloaded 01/31/22 08:20 PM UTC

the 1991-1993 El Niño. *J. Geophys. Res.*, **100**, 6881–6898, https://doi.org/10.1029/94JC03312.

Liu, C., A. Kohl, Z. Liu, F. Wang, and D. Stammer, 2016: Deep-reaching thermocline mixing in the equatorial Pacific cold tongue. *Nat. Commun.*, **7**, 11576, https://doi.org/10.1038/ncomms11576.

McPhaden, M. J., 1995: The Tropical Atmosphere Ocean array is completed. *Bull. Amer. Meteor. Soc.*, **76**, 739–744, https://doi.org/10.1175/1520-0477-76.5.739.

——, and J. Picaut, 1990: El Niño-Southern Oscillation displacements of the western equatorial Pacific warm pool. *Science*, **250**, 1385–1388, https://doi.org/10.1126/science.250.4986.1385.

——, and Coauthors, 1998: The Tropical Ocean-Global Atmosphere observing system: A decade of progress. *J. Geophys. Res.*, **103**, 14 169–14 240, https://doi.org/10.1029/97JC02906.

Moum, J., and D. Caldwell, 1985: Local influences on shear flow turbulence in the equatorial ocean. *Science*, **230**, 315–316, https://doi.org/10.1126/science.230.4723.315.

——, and J. Nash, 2009: Mixing measurements on an equatorial ocean mooring. *J. Atmos. Oceanic Technol.*, **26**, 317–336, https://doi.org/10.1175/2008JTECHO617.1.

——, D. Caldwell, and C. Paulson, 1989: Mixing in the equatorial surface layer and thermocline. *J. Geophys. Res.*, **94**, 2005–2021, https://doi.org/10.1029/JC094iC02p02005.

——, D. Hebert, C. A. Paulson, and D. R. Caldwell, 1992: Turbulence and internal waves at the equator. Part I: Statistics from towed thermistors and a microstructure profiler. *J. Phys. Oceanogr.*, **22**, 1330–1345, https://doi.org/10.1175/1520-0485(1992)022<1330:TAIWAT>2.0.CO;2.

——, R.-C. Lien, A. Perlin, J. Nash, M. Gregg, and P. Wiles, 2009: Sea surface cooling at the equator by subsurface mixing in tropical instability waves. *Nat. Geosci.*, **2**, 761–765, https://doi.org/10.1038/ngeo657.

——, A. Perlin, J. Nash, and M. McPhaden, 2013: Ocean mixing controls seasonal sea surface cooling in the equatorial Pacific cold tongue. *Nature*, **500**, 64–67, https://doi.org/10.1038/nature12363.

Osborn, T. R., 1980: Estimates of the local rate of vertical diffusion from dissipation measurements. *J. Phys. Oceanogr.*, **10**, 83–89, https://doi.org/10.1175/1520-0485(1980)010<0083:EOTLRO>2.0.CO;2.

——, and C. S. Cox, 1972: Oceanic fine structure. *Geophys. Fluid Dyn.*, **3**, 321–345, https://doi.org/10.1080/03091927208236085.

Pacanowski, R., and S. Philander, 1981: Parameterization of vertical mixing in numerical models of tropical oceans. *J. Phys. Oceanogr.*, **11**, 1443–1451, https://doi.org/10.1175/1520-0485(1981)011<1443:POVMIN>2.0.CO;2.

Perlin, A., and J. Moum, 2012: Comparison of thermal dissipation rate estimates from moored and profiling instruments at the equator. *J. Atmos. Oceanic Technol.*, **29**, 1347–1362, https://doi.org/10.1175/JTECH-D-12-00019.1.

Peters, H., M. Gregg, and J. O'Toole, 1988: On the parameterization of equatorial turbulence. *J. Geophys. Res.*, **93**, 1199–1218, https://doi.org/10.1029/JC093iC02p01199.

Pham, H. T., S. Sarkar, and K. Winters, 2013: Large-eddy simulation of deep-cycle turbulence in an upper-equatorial undercurrent model. *J. Phys. Oceanogr.*, **43**, 2490–2502, https://doi.org/10.1175/JPO-D-13-016.1.

——, W. D. Smyth, S. Sarkar, and J. N. Moum, 2017: Seasonality of deep cycle turbulence in the eastern equatorial Pacific. *J. Phys. Oceanogr.*, **47**, 2189–2209, https://doi.org/10.1175/JPO-D-17-0008.1.

Praveen Kumar, B., J. Vialard, M. Lengaigne, V. S. N. Murty, M. J. McPhaden, M. Cronin, F. Pinsard, and K. G. Reddy, 2013: TropFlux wind stresses over the tropical oceans: Evaluation and comparison with other products. *Climate Dyn.*, **40**, 2049–2071, https://doi.org/10.1007/s00382-012-1455-4.

Press, W., S. Teukolsky, W. Vetterling, and B. Flannery, 1992: *Numerical Recipes in Fortran: The Art of Scientific Computing.* 2nd ed. Cambridge University Press, 963 pp.

Price, J., R. Weller, and R. Pinkel, 1986: Diurnal cycling: Observations and models of the upper ocean's response to diurnal heating, cooling and wind mixing. *J. Geophys. Res.*, **91**, 8411–8427, https://doi.org/10.1029/JC091iC07p08411.

Smyth, W. D., 2020: Marginal instability and the efficiency of ocean mixing. *J. Phys. Oceanogr.*, **50**, 2141–2150, https://doi.org/10.1175/JPO-D-20-0083.1.

——, J. Moum, L. Li, and S. Thorpe, 2013: Diurnal shear instability, the descent of the surface shear layer, and the deep cycle of equatorial turbulence. *J. Phys. Oceanogr.*, **43**, 2432–2455, https://doi.org/10.1175/JPO-D-13-089.1.

——, H. T. Pham, J. N. Moum, and S. Sarkar, 2017: Pulsating turbulence in a marginally unstable stratified shear flow. *J. Fluid Mech.*, **822**, 327–341, https://doi.org/10.1017/jfm.2017.283.

——, J. Nash, and J. Moum, 2019: Self-organized criticality in geophysical turbulence. *Sci. Rep.*, **9**, 3747, https://doi.org/10.1038/s41598-019-39869-w.

Thorpe, S., and Z. Liu, 2009: Marginal instability? *J. Phys. Oceanogr.*, **39**, 2373–2381, https://doi.org/10.1175/2009JPO4153.1.

Warner, S. J., and J. N. Moum, 2019: Feedback of mixing to ENSO phase change. *Geophys. Res. Lett.*, **46**, 13 920–13 927, https://doi.org/10.1029/2019GL085415.

Zaron, E., and J. Moum, 2009: A new look at Richardson number mixing schemes for equatorial ocean modeling. *J. Phys. Oceanogr.*, **39**, 2652–2664, https://doi.org/10.1175/2009JPO4133.1.

Brought to you by OREGON STATE UNIVERSITY | Unauthenticated | Downloaded 01/31/22 08:20 PM UTC